

Jupiter internal structure: the effect of different equations of state

Y. Miguel¹ T. Guillot¹ and L. Fayon^{2,3}

¹ Laboratoire Lagrange, UMR 7293, Université de Nice-Sophia Antipolis, CNRS, Observatoire de la Côte d'Azur, Blvd de l'Observatoire, CS 34229, 06304 Nice cedex 4, France

e-mail: yamila.miguel@oca.eu

² Institut de Physique du Globe de Paris, 1 Rue Jussieu, 75005 Paris, France

³ AstroParticule et Cosmologie, 10 Rue Alice Domon et Leonie Duquet, 75013 Paris, France

October 28, 2021

ABSTRACT

Context. Heavy elements, even though its smaller constituent, are crucial to understand Jupiter formation history. Interior models are used to determine the amount of heavy elements in Jupiter interior, nevertheless this range is still subject to degeneracies due to uncertainties in the equations of state.

Aims. Prior to Juno mission data arrival, we present Jupiter optimized calculations exploring the effect of different model parameters in the determination of Jupiter's core and heavy element's mass. We perform comparisons between equations of state published recently.

Methods. The interior model of Jupiter is calculated from the equations of hydrostatic equilibrium, mass and energy conservation, and energy transport. The mass of the core and heavy elements is adjusted to match Jupiter's observational constrains radius and gravitational moments.

Results. We show that the determination of Jupiter interior structure is tied to the estimation of its gravitational moments and the accuracy of equations of state of hydrogen, helium and heavy elements. The location of the region where Helium rain occurs as well as its timescale are important to determine the distribution of heavy elements and helium in the interior of Jupiter. We show that differences find when modeling Jupiter's interior with recent EOS are more likely due to differences in the internal energy and entropy calculation. The consequent changes in the thermal profile lead to different estimations of the mass of the core and heavy elements, explaining differences in recently published Jupiter interior models.

Conclusions. Our results help clarify differences find in Jupiter interior models and will help the interpretation of upcoming Juno data.

Key words. Planets and satellites: composition

1. Introduction

Jupiter's internal structure is estimated with interior models which use observational constrains such as its mass, radius and gravitational moments, derived from measurements made with Pioneer and Voyager (Campbell & Synnott 1985). Juno mission is designed to improve our knowledge of Jupiter's interior and its formation history by a combination of highly accurate measurements of Jupiter's gravity and magnetic field as well as water abundance in the atmosphere.

Models of Jupiter's internal structure rely on the study of the properties of hydrogen and helium at high pressures (Saumon & Guillot 2004; Fortney & Nettelmann 2010; Baraffe et al. 2014). One of the most successful equations of state was the one published by Saumon et al. (1995) (SCvH) which has been used in numerous publications for giant planet's interior calculations. Since 1995, development in numerical techniques allowed a new generation of equations of state calculated from *Ab initio* simulations (Nettelmann et al. 2008; Militzer et al. 2008; Militzer 2006, 2009; Caillabet et al. 2011; Nettelmann et al. 2012; Militzer & Hubbard 2013; Becker et al. 2014). These equations of state, even though calculated from the same principles and numerical techniques, were used to construct Jupiter interior models with different results.

While results by Nettelmann et al. (2008) suggested small core masses up to $8 M_{Earth}$ consistent with previous estimations

(Saumon & Guillot 2004), results by Militzer et al. (2008) challenged the small core hypothesis finding large cores of $14-18 M_{Earth}$. Nettelmann et al. (2012) improved their previous model and equation of state (Nettelmann et al. 2008), and tested different models for the distribution of heavy elements in Jupiter's interior. They found that a Jupiter model with an homogenous interior plus a core will lead to larger cores more consistent with Militzer et al. (2008) estimations, while a discontinuous distribution of helium and heavy elements plus a core leads to core masses of up to $8 M_{Earth}$ but a large mass of heavy elements ($28-32 M_{Earth}$). They concluded that the differences in Jupiter internal structure originate from different model assumptions, a conclusion in agreement with Militzer & Hubbard (2009) analysis. After those papers two new results were published. Militzer & Hubbard (2013) (MH13) present a new equation of state for an interacting hydrogen-helium mixture with self consistent entropy calculations and a recent paper by Becker et al. (2014) (REOS.3) shows updated tables for hydrogen and helium in a large range which covers all temperatures and densities in Jupiter's interior. These recent estimations still present differences in Jupiter interior calculations, showing that one of the big challenges in the modeling of Jupiter's internal structure still rests on the determination and accuracy of hydrogen and helium equations of state.

We explore the differences in the internal structure of Jupiter -on its derived core and heavy elements' mass- calculated with the same model assumptions but different equations of state, exploring also the effect of different equations of state for heavy elements, different locations of the separation between the molecular and metallic layer and different models for the heavy elements' distribution in Jupiter's interior. In anticipation of Juno measurements, we also study the gravitational moments used to constrain the solutions, to get a better knowledge of the sensitivity of Jupiter interior to different model parameters and understand the implications of Juno measurements in internal structure calculations.

2. Modeling Jupiter

Jupiter's internal structure is determined from the equations of hydrostatic equilibrium, mass and energy conservation, and energy transport, which are calculated using the code CEPAM (Guillot & Morel 1995). We set the boundary condition at 1 bar to be $T=165\text{K}$ from Voyager and Galileo measurements (Lindal 1992; Atkinson et al. 1998), where the mass and luminosity are almost equal to the total mass and luminosity of the planet. In this work, we assume that the envelope structure is adiabatic. We note that the presence of deep radiative zones is unlikely (see Guillot et al. (2004)). Some recent work include a non-adiabatic, double-diffusive region in the helium demixing region (Nettelmann et al. 2015; Mankovich et al. 2016), but this has an effect on the inferred core mass and mass of heavy elements that is significantly smaller than the uncertainties discussed here. We do not consider the possibility that the envelope is entirely double-diffusive, a possibility that would yield vastly larger amounts of heavy elements in the interior (Leconte & Chabrier 2012). We note that dry Ledoux convection tends to homogenize a large fraction of the envelope (Vazan et al. 2016), implying that this possibility is unlikely.

Helium abundance in the external envelope is taken as $Y = 0.238 \pm 0.007$ to match the in situ observations made by the Galileo probe (Zahn et al 1998). To explain helium depletion compared to the protosolar value (0.270 ± 0.005 , Bahcall & Pinsonneault (1995)) we assume that a helium phase transition occurs at a pressure P_{sep} , between 0.8 and 4 Mbar according to Morales et al. (2013) immiscibility calculations. Helium settles down increasing the abundance at the deeper layer, which accounts for the depleted amount in the outer envelope. Since the physics and dynamics of helium rain is not understood in detail, we consider two different models for the distribution of solids in the planet's interior. In one model helium rain has a fast timescale allowing an efficient mixture of solids in the interior of Jupiter, which has an homogeneous distribution (Z-homogeneous). In the other model we assume that helium rain induces a compositional difference between the two layers and therefore in this scenario there are two different abundances for the metals in the outer and deeper layer (Z-discontinuous).

3. Equations of state

3.1. Hydrogen and helium

The proper determination of Jupiter's internal structure is tied to the accuracy of the equations of state at the range of temperatures and pressures reached in the interior of this giant. Since $\sim 85\%$ of Jupiter's mass is hydrogen and helium, the equations of state of these elements determine its internal structure. Nevertheless, we show that the treatment adopted for the heavy elements also

affects the core mass and total mass of heavy elements retrieved with our calculations (section 4.2.2).

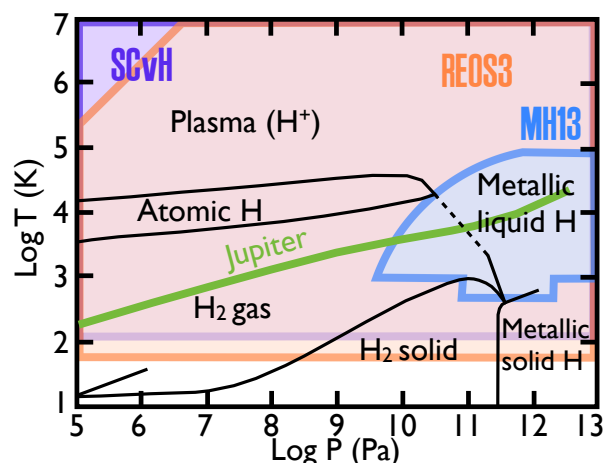


Fig. 1. Phase diagram of hydrogen (adapted from Guillot & Gautier (2015)). The range of validity of each equation of state in the range of the figure is shown in different colors: SCvH is shown in purple, MH13 in blue and REOS.3 in orange. Jupiter's internal structure is shown (green thick line).

In this study we use three different equations of state for hydrogen and helium: the widely used Saumon et al. (1995) equations of state, and the more recent equations of state derived from *Ab initio* calculations published by Militzer & Hubbard (2013) and by Becker et al. (2014). Figure 1 shows the phase diagram of hydrogen and the range of pressure and temperature covered by each equation of state.

3.1.1. A pure hydrogen equation of state from MH13 results

MH13 table has pressure, internal energy, Helmholtz free energy and specific entropy as function of density and temperature, while CEPAM uses tables where entropy and density are given as function of pressure and temperature. We use cubic spline interpolation to create a table in CEPAM format.

As shown in figure 1, MH13 equation of state was made for a small range of pressure and temperature that do not cover all pressures and temperatures in Jupiter's interior. We extend the table using SCvH equation of state for those temperatures and pressures with no data. To smoothen the limits between the two tables we use linear interpolation. The new table covers a range of pressure between 10^4 and 10^{19} $\text{g}/(\text{cm}^2)$ and a range of temperatures $2.25 \leq \text{Log}(T) \leq 7$ K.

MH13 equation of state was made for a mixture of hydrogen and helium ($Y_{MH13}=0.245$). To allow a change in the composition of the molecular and metallic envelopes, we extracted the hydrogen from the table, creating a pure hydrogen equation of state based on MH13 results. We calculated density and entropy for each pressure and temperature in the table using the equations for a mixture and the SCvH equation of state for helium:

$$\frac{1}{\rho_H} = \frac{1}{X_{MH13}} \left(\frac{1}{\rho_{MH13}} - \frac{Y_{MH13}}{\rho_{SCvH,He}} \right) \quad (1)$$

$$S_H = \frac{1}{X} (S_{MH13} - Y S_{SCvH,He}) \quad (2)$$

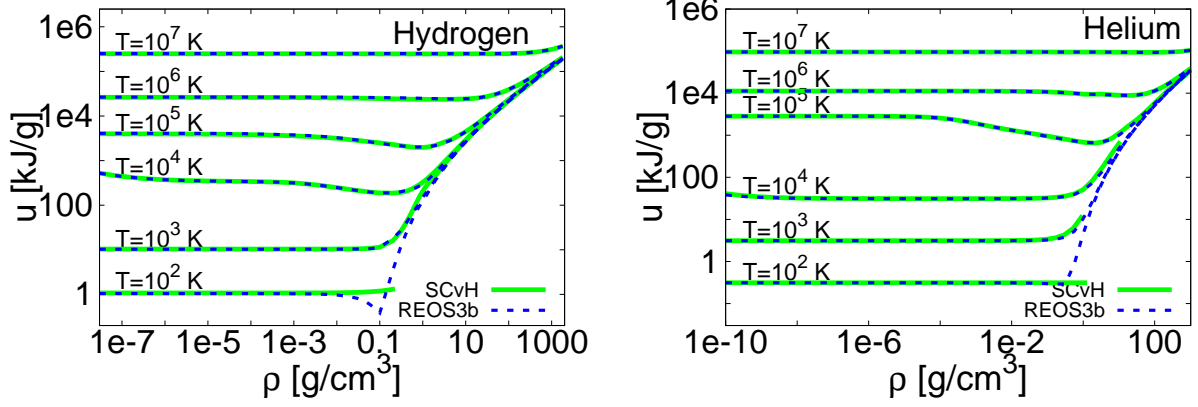


Fig. 2. Specific internal energy as a function of density at different temperatures for hydrogen (left panel) and helium (right panel), using two different equations of state. SCvH is shown in green solid lines and the values shown in blue dotted lines correspond to the u in REOS.3 plus Δu ($\Delta u_H = 1590.12135$ for hydrogen and $\Delta u_{He} = 1843.06795$ for helium) or REOS3b.

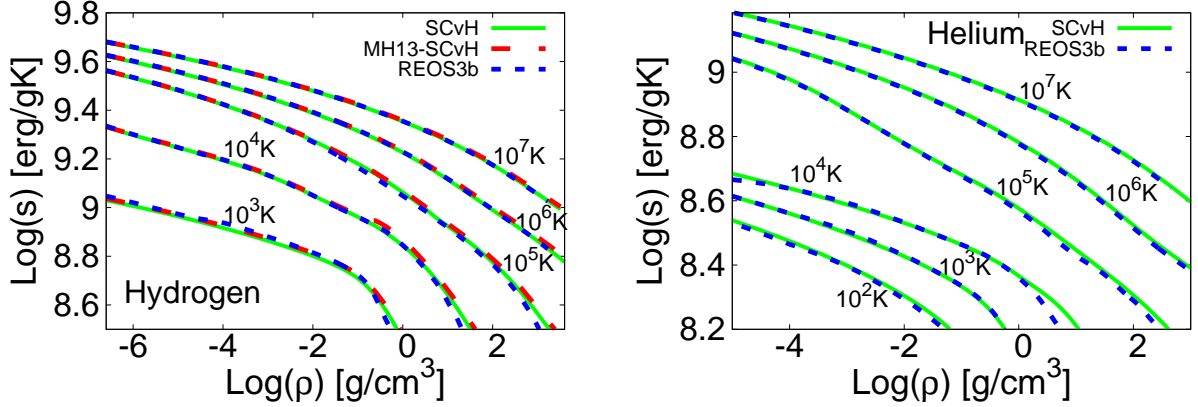


Fig. 3. Specific entropy vs. density at different temperatures for hydrogen (left panel) and helium (right panel). For hydrogen we show a comparison between the entropy calculated with REOS3b (blue), the one published in SCvH (green) and MH13+SCvH values (red). Since MH13+SCvH is a pure hydrogen table, the right panel shows a comparison between REOS3b and SCvH only.

with ρ_H and S_H the density and entropy of the pure hydrogen equation of state we extracted from MH13 table, $\rho_{SCvH,He}$ and $S_{SCvH,He}$ the density and entropy in the SCvH helium table, X_{MH13} , ρ_{MH13} and S_{MH13} the hydrogen mass fraction, density and entropy in MH13, respectively. Eq. (2) neglects the entropy of mixing. Detailed calculations using the SCvH EOS with and without this entropy of mixing show that this is a much smaller effect than the uncertainties on the EOSs themselves discussed here. We call this new hydrogen table MH13+SCvH (shown in appendix A).

3.1.2. Entropy calculation for hydrogen and helium using REOS.3

REOS.3 is a density-temperature equation of state with pressure and specific internal energy that covers a large range in pressure and temperature (figure 1, for hydrogen). To allow comparisons between the tables and avoid errors in the entropy calcu-

lation, we changed the zero point of the specific internal energy in the REOS.3 tables to make them coincide in the ideal gas regime with the SCvH EOS (N. Nettelmann and A. Becker private communication). Since the difference between the specific internal energy of REOS.3 and SCvH equations of state at $T=60$ K and $\rho = 10^{-3}$ g/cm³ is $\Delta u_H = 1590.12135$ for hydrogen and $\Delta u_{He} = 1843.06795$ for helium, we added these values to all the specific internal energies in the REOS.3 H and He tables, respectively. Figure 2 shows a comparison between the internal energies of SCvH and REOS.3 + Δu .

The entropy is a necessary parameter in internal structure calculations. The two layers considered in the model follow an adiabat, therefore the ratio between the derivatives of the entropy with respect to pressure and temperature gives us the temperature gradient in the planet's interior. We calculate the specific entropy, s , for each point of the REOS.3 table through thermodynamic relations between the published u , P , T and ρ (Nettelmann et al. 2012).

From the definition of the Helmholtz free energy:

$$F = U - TS$$

it follows,

$$s(T, V) = \frac{u(T, V)}{T} - \frac{1}{M} \left(\frac{F(T, V)}{T} - \frac{F(T_0, V_0)}{T_0} \right) + s_0 \quad (4)$$

Since,

$$\frac{1}{M} \left(\frac{F(T, V)}{T} - \frac{F(T_0, V_0)}{T_0} \right) = \frac{1}{M} \int_{T_0, V_0}^{T, V} d \left(\frac{F(T', V')}{T'} \right) \quad (5)$$

and

$$d \left(\frac{F(T', V')}{T'} \right) = \frac{dF}{T'} - \frac{F}{T'^2} dT' \quad (6)$$

from Eq. (3) it follows,

$$\frac{dF}{T'} = \frac{d(U - TS)}{T'} = \frac{dU}{T'} - dS - \frac{S}{T'} dT' \quad (7)$$

and

$$\frac{F}{T'^2} dT' = \frac{(U - TS)}{T'^2} dT' \quad (8)$$

then Eq. (6) can be written as:

$$d \left(\frac{F(T', V')}{T'} \right) = \frac{dU}{T'} - dS - \frac{U}{T'^2} dT' \quad (9)$$

using that

$$\frac{dU}{T'} = -\frac{P}{T'} dV + dS \quad (10)$$

then

$$d \left(\frac{F(T', V')}{T'} \right) = -\frac{P}{T'} dV - \frac{U}{T'^2} dT' \quad (11)$$

Now, going to ρ and T plane

$$\frac{1}{M} d \left(\frac{F(T', \rho')}{T'} \right) = \frac{P}{T'} \frac{1}{\rho'^2} d\rho' - \frac{u}{T'^2} dT' \quad (12)$$

Finally,

$$\frac{1}{M} \int_{T_0, \rho_0}^{T, \rho} d \left(\frac{F(T', \rho')}{T'} \right) = \int_{\rho_0}^{\rho} \frac{P(T_0, \rho')}{T_0} \frac{1}{\rho'^2} d\rho' - \int_{T_0}^T \frac{u(T', \rho)}{T'^2} dT' \quad (13)$$

and going back to Eq. (4):

$$s(T, \rho) = \frac{u(T, V)}{T} - \left[\int_{\rho_0}^{\rho} \frac{P(T_0, \rho')}{T_0} \frac{1}{\rho'^2} d\rho' - \int_{T_0}^T \frac{u(T', \rho)}{T'^2} dT' \right] + s_0 \quad (14)$$

The specific entropy at each point is calculated from Eq. (14), using the trapezoid rule for the numerical integration and cubic splines interpolation to add temperature and density points to improve the numerical calculation. Figure 3 shows a comparison of the entropy calculated at different temperatures with other equations of state.

These new equations of state with entropy and internal energies that coincide with SCvH at $T=60$ K and $\rho = 10^{-3}$ g/cm³ are called REOS3b (see appendix A).

3.2. Comparison with experiments

(3) The original equations of state MH13 and REOS.3 experienced some changes such as the creation of a pure hydrogen table and the extension of such table for a large pressure and temperature range (MH13+SCvH, section 3.1.1), the change of the u_0 and entropy calculation (REOS3b section 3.1.2), and interpolation to add more points and make a pressure-temperature table (MH13+SCvH and REOS3b). In order to test our final tables, we make comparisons with high pressure experiments.

A lot of attention has been devoted to experiments designed to understand the properties of hydrogen (or deuterium) and helium at high densities (Nellis et al. 1983, 1984; Holmes et al. 1995; Collins et al. 1998; Belov et al. 2002; Boriskov et al. 2003; Grishechkin et al. 2004; Knudson et al. 2004; Eggert et al. 2008; Hicks et al. 2009; Celliers et al. 2010; Loubeyre et al. 2012). In these experiments a gas at rest with an initial thermodynamic state (u_0, ρ_0, P_0) is exposed to an abrupt change in pressure, temperature and density. Applying the laws of conservation of mass, momentum and energy at both sides of this shock wave, we derive a relation between the state of the gas before and after the shock, called the Rankine-Hugoniot equation:

$$H(\rho, P) = u - u_0 + \frac{1}{2} (P + P_0) \left(\frac{1}{\rho} - \frac{1}{\rho_0} \right) \quad (15)$$

where ρ, P, u are the density, pressure and internal energy of the final shocked gas. Equation 15 defines all states on the (u, ρ, P) surface that can be reached from the initial condition by a single shock.

3.2.1. Hugoniot-curve calculation from P, T, ρ and s

The Hugoniot curve, $H(\rho, P)$, is defined by:

$$H(\rho, P) = 0 \quad (16)$$

Since our EOS tables give us P, T, ρ and s we want to write Eq. (16) as a function of these variables. If we differentiate Eq. (16) we obtain:

$$dH = du + \frac{1}{2} \left[\left(\frac{1}{\rho} - \frac{1}{\rho_0} \right) dP - \left(\frac{1}{\rho^2} (P + P_0) d\rho \right) \right] = 0 \quad (17)$$

Now we know that:

$$du = -P dV + T ds \quad (18)$$

where $V = \frac{1}{\rho}$ and therefore,

$$dV = -\frac{d\rho}{\rho^2} \quad (19)$$

Using Eq. (18) and (19) in (17):

$$dH = \frac{1}{2} \left(\frac{1}{\rho} - \frac{1}{\rho_0} \right) dP + \frac{1}{2} \frac{(P - P_0)}{\rho^2} d\rho + T ds = 0 \quad (20)$$

to integrate in the P,T plane, we use:

$$d\rho(P, T) = \frac{\partial \rho(P, T)}{\partial P} dP + \frac{\partial \rho(P, T)}{\partial T} dT \quad (21)$$

$$ds(P, T) = \frac{\partial s(P, T)}{\partial P} dP + \frac{\partial s(P, T)}{\partial T} dT \quad (22)$$

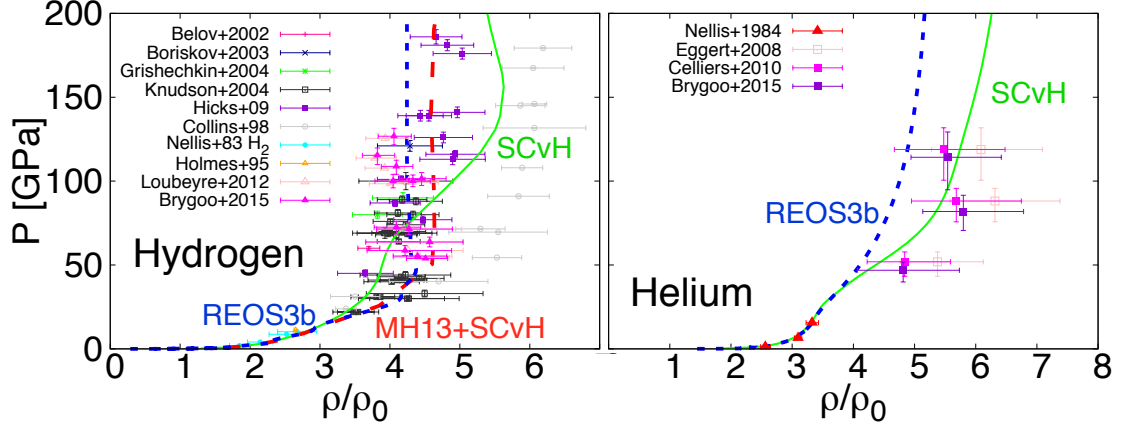


Fig. 4. Principal Hugoniot of hydrogen (left panel) and helium (right panel). The curves were calculated for an initial state of $\rho_0 = 0.0855 \text{ g/cm}^3$ and $T_0 = 20 \text{ K}$ for hydrogen and $\rho_0 = 0.123 \text{ g/cm}^3$ and $T_0 = 4 \text{ K}$ for helium. Experimental results are shown with different point styles for comparison. We included recent estimations by Brygoo et al. (2015) who presented corrections of previously published data on He (Eggert et al. 2008; Celliers et al. 2010), H_2 and D_2 (Loubeyre et al. 2012) based on a better understanding of shocked compressed SiO_2 .

Equation (20) is written as:

$$dH(P, T) = \frac{1}{2} \left(\frac{1}{\rho(P, T)} - \frac{1}{\rho_0} \right) dP + \frac{1}{2} \frac{(P - P_0)}{\rho(P, T)^2} \frac{\partial \rho(P, T)}{\partial P} dP + \frac{1}{2} \frac{(P - P_0)}{\rho(P, T)^2} \frac{\partial \rho(P, T)}{\partial T} dT + T \frac{\partial s(P, T)}{\partial P} dP + T \frac{\partial s(P, T)}{\partial T} dT \quad (23)$$

Integrating Eq. (23) between an initial point and the final state, we get the Hugoniot curve as a function of the variables present in our EOS tables:

$$H(P, T) - H_0 = \frac{1}{2} \int_{P(H_0)}^P \left(\frac{1}{\rho(P, T(H_0))} - \frac{1}{\rho_0} \right) dP + \frac{1}{2} \int_{P(H_0)}^P \frac{(P - P_0)}{\rho(P, T(H_0))^2} \frac{\partial \rho(P, T(H_0))}{\partial P} dP + \int_{P(H_0)}^P T(H_0) \frac{\partial s(P, T(H_0))}{\partial P} dP + \frac{1}{2} \int_{T(H_0)}^T \frac{(P - P_0)}{\rho(P, T)^2} \frac{\partial \rho(P, T)}{\partial T} dT + \int_{T(H_0)}^T T \frac{\partial s(P, T)}{\partial T} dT \quad (24)$$

To find the zeros in Eq. (24) we calculate $H(P, T)$ at each P and T in the EOS table and when it changes sign we do a cubic spline interpolation in P and T to find the exact values of P, T , $\rho(P, T)$ and $s(P, T)$ that will give us $H(P, T) = 0$. Figure 4 shows Hugoniot curves for hydrogen and helium obtained when using different equations of state and compared with experimental data.

3.3. Heavy elements

Hydrogen and helium are the most relevant species, but an accurate description of Jupiter's interior needs a definition of the heavy elements equation of state. In our model heavy elements are water and rocks, and we use three different equations of state to test their sensitivity. Following Saumon & Guillot (2004) we use for rocks the equation of state for a mixture of silicates called "dry sand" in SESAME (Lyon & Johnson 1992). For water we

use the SESAME EOS (Lyon & Johnson 1992), and a more recent equation of state calculated in Valencia et al. (2013), which combines an equation of state for water at high temperatures ($T > 1000 \text{ K}$) (French et al. 2009) with results taken from NIST database (Saul & Wagner 1989).

4. Results

4.1. Different thermal structures

In this section we make a comparison of Jupiter's interior with different equations of state. Figure 5 shows that REOS3b leads to larger temperatures for all densities compared to the other two equations of state. The differences are large even at relatively low densities, being close to 1000 K for $\rho \approx 0.2 \text{ g/cm}^3$. Since MH13+SCvH uses SCvH equation of state for densities $\rho < 0.22246 \text{ g/cm}^3$, the differences between these two EOS arise for large densities, where MH13+SCvH reaches lower temperatures. These differences in the thermal profiles explain the different mass of metals in the envelope and mass of the core derived with the optimized models.

4.2. Optimized models

We calculate optimized models of Jupiter, in which the abundance of heavy elements and the mass of the core (M_{core}), are adjusted to reproduce the observables within their error bars (see Guillot et al. (1994) for more details on the method).

4.2.1. Jupiter's gravitational moments

Our models match Jupiter's radius and gravitational moments J_2 and J_4 . These last ones, have changed with time according we improved our knowledge on Jupiter's gravity field. Table 1 shows the gravitational moments adopted in this paper. We consider gravitational moments derived from pre-Juno observations by Voyager 1 and 2, Pioneer 10 and 11 (Campbell & Synnott 1985), as well as more recent values derived from JUP230 and

Table 1. Gravitational moments explored.

J_2 [$\times 10^{-2}$]	J_4 [$\times 10^{-4}$]	J_6 [$\times 10^{-5}$]	Note	Reference
1.4697 (0.0001)	-5.84 (0.05)	3.10 (2)	Pre-Juno observed J_s	Campbell & Synnott (1985)
1.4682 (0.0001)	-5.80 (0.05)	3.04 (2)	J_s with differential rotation	Guillot (1999)
1.469643 (0.000021)	-5.8714 (0.0168)	3.425 (0.522)	JUP230 orbit solution	Jacobson (2003)
1.469562 (0.000029)	-5.9131 (0.0206)	2.078 (0.487)	JUP310 orbit solution	Jacobson (2013)

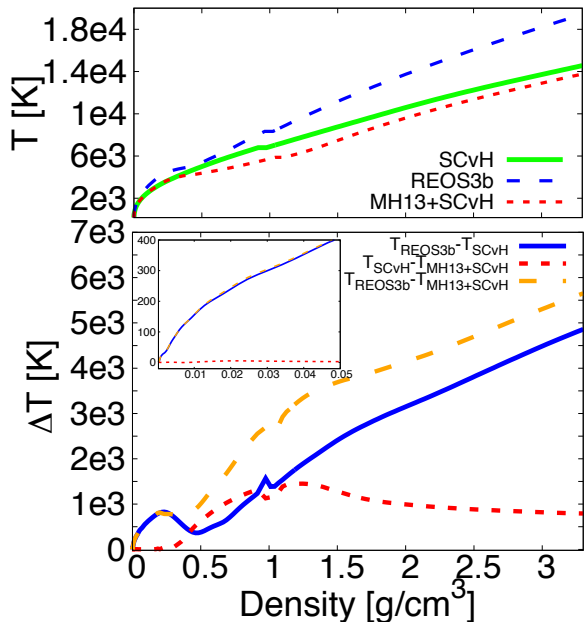


Fig. 5. Top panel: Jupiter’s density and temperature for different equations of state: SCvH (green solid), REOS3b (blue dashed) and MH13+SCvH (red dotted line). The discontinuity is due to the separation of the outer and deeper envelope at $P_{sep} = 1$ Mbar. Bottom panel: differences in the temperature obtained with the three different equations of state. Blue line is the temperature difference between REOS3b and SCvH, red dotted line is the difference between SCvH and MH13+SCvH and orange dashed is the difference between REOS3b and MH13+SCvH.

JUP310 orbit solutions¹, and also values with a correction by differential rotation effects, where Hubbard (1982) solution to the planetary figure problem was adopted in case of a deep rotation field with cylindrical symmetry (Guillot 1999).

Our calculation of the gravitational moments is based on the theory of figures of 4th order. A comparison with more detailed calculations made with concentric Maclaurin spheroid (Hubbard 2012, 2013) (W. B. Hubbard and N. Movshovitz, private communication) showed that our approximation leads to an error of the order of $1e-7$ in J_4 and $2e-6$ in J_6 . Figure 6 shows gravitational moments of order 4 and 6 as well as the resulting J_s in all our optimized models with different equations of state. The black arrow shows the error in the determination of J_6 . The observed J_s change when considering differential rotation (indicated with the grey arrow in the Figure). Further studies including interior dynamics will help improve our understanding of Jupiter interior from gravity measurements (Kaspi et al. 2010; Galanti & Kaspi 2016).

¹ Values calculated by Jacobson, R. A. in 2003 and 2013, respectively and published in the JPL website:

http://ssd.jpl.nasa.gov/?gravity_fields_op

The results of our simulations are very confined in the J_4 - J_6 diagram, specially in the case of J_6 which is narrowly defined within this framework. We find larger $|J_4|$ and J_6 than observed values and the most recent estimations of 2013. Our results with MH13+SCvH and a recent estimation by Hubbard & Militzer (2016) show a similar tendency towards preferred J_4 and J_6 values.

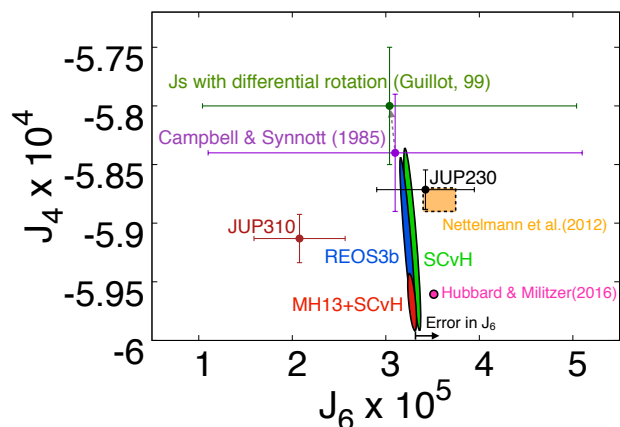


Fig. 6. J_4 and J_6 pre-Juno observed values (Campbell & Synnott 1985) (purple), those with a correction due to differential rotation (Guillot 1999) (dark green) and more recent estimations by Jacobson in 2003 (black) and 2013 (brown). J_s solutions of our optimized models within 2σ of Campbell & Synnott (1985) and modeled with Z-discontinuous are shown in different colors according to the equation of state used in the simulation: SCvH (green), REOS3b (blue) and MH13+SCvH (red). Pink dot shows a recent model by Hubbard & Militzer (2016) and orange box shows estimations by Nettelmann et al. (2012) for comparison.

In our models Y_{deep} is calculated to account for the missing helium in Jupiter’s atmosphere respect to the protosolar value (section 2). Figure 7 shows J_4 , J_6 and M_Z found in our optimized models when changing Y_{proto} and maintaining Y_{atm} fixed, to test the effect of changing the abundance of helium in Jupiter’s deep layer. To satisfy the constrain in J_2 , larger Y_{deep} leads to lower mass of heavy elements in the envelope, which decreases approximately $5 M_{Earth}$ when going from $Y_{deep} = 0.238$ to $Y_{deep} = 0.28$ in all cases. Larger abundance of helium in the deep layer ensures solutions closer to current J_4 and J_6 estimations.

The mass of the core and the mass of heavy elements found in our models depend on the J_s used to constrain the solutions. Figure 8 shows that solutions find with J_s derived from observations published by Campbell & Synnott (1985) lead to larger M_{core} and smaller M_Z than the values find with more recent estimations by Jacobson (2003; 2013). M_{core} estimations when using J_s by Campbell & Synnott (1985) reach core masses $4M_{Earth}$ larger than the values find with J_s by Jacobson (2003) for REOS3b and SCvH. The lowest M_Z find with J_s by Campbell & Synnott (1985) are $6M_{Earth}$ lower than estimations find with

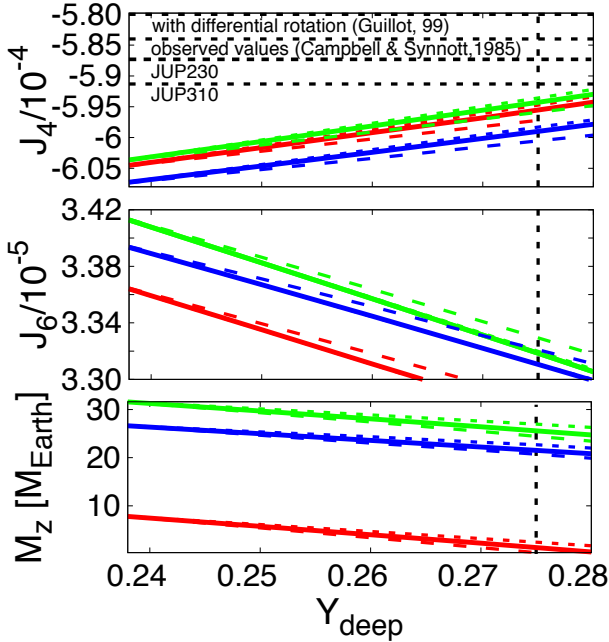


Fig. 7. Model results when adjusting the mass of the core and heavy elements to reproduce Jupiter’s radius and J_2 . In these models the atmospheric helium mass mixing ratio is fixed to $Y_{atm} = 0.238$ and we change the helium abundance in the deeper layer to match the protosolar value within its error bars. Different panels show J_4 (upper panel), J_6 (middle panel) and M_Z (lower panel). Different colors show results for the three different equations of state of hydrogen and helium: SCvH (green), MH13+SCvH (red) and REOS3b (blue). The lines indicate different locations of the helium phase that separates the two envelopes at 0.8 Mbar (dashed), 2 Mbar (solid) and 4 Mbar (dotted lines). The vertical dashed line indicate the protosolar helium mixing ratio and the horizontal lines in the upper panel show estimations of J_4 from observations and models as a reference.

values calculated by Jacobson (2003) for REOS3b and SCvH. Results found with MH13+SCvH do not change significantly for M_Z but there is a difference of $2M_{Earth}$ in M_{core} in the solutions estimated with the different J_s . There are no solutions found within 2σ with J_s estimated by Jacobson (2003). New information provided by Juno will contribute to more accurate data to calculate gravitational moments of larger order and improve the uncertainty in lower ones, towards a better determination of Jupiter internal structure.

4.2.2. Jupiter’s core and heavy element’s mass

For the following optimized models we adjusted our solutions to reproduce Jupiter’s radius, J_2 and J_4 . For Z-homogeneous cases we adjust the core mass and heavy elements mass mixing ratio, while for Z-discontinuous we find the difference between the abundance of heavy elements in the outer and deeper envelope (ΔZ) and core mass that best reproduce the observables. Our baseline models were made using J_2 and J_4 derived from observations of Jupiter gravity field (Campbell & Synnott 1985), $P_{sep} = 2$ Mbar and the NIST equation of state for hot H_2O as the equation of state for heavy elements. Models that differ from these conditions are indicated in the text and figure captions. We consider uncertainties in the averaged helium mass mixing ratio, the atmospheric helium mass mixing ratio, the mass mixing ratio of rocks and ices and the ice fraction in the core. Due to these uncertainties our range of potential solutions cover an area in the

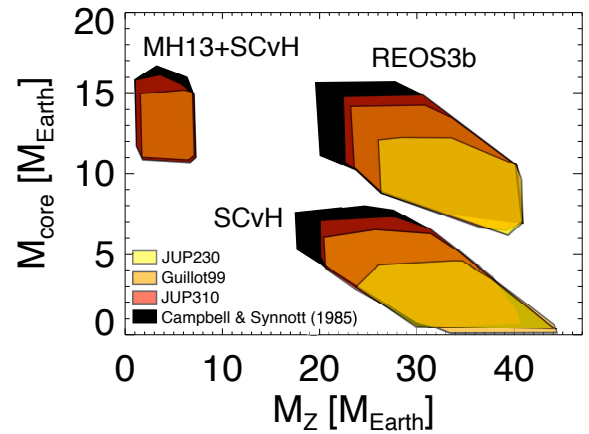


Fig. 8. Mass of the core and heavy elements in Jupiter interior derived with different J_s . Models use Z-discontinuous scenario, $P_{sep} = 2$ Mbar and different EOS indicated in the figure. Colored areas shows solutions within 2σ from Jupiter’s radius, J_2 and J_4 estimated by Campbell & Synnott (1985) (black), Guillot (1999) (orange), Jacobson (2003) (yellow) and Jacobson (2013) (red). No solution was found with MH13+SCvH and constrains by JUP230.

M_{core} - M_Z diagram. In addition, we explore different values of J_2 and J_4 (see table 1), different equations of state for heavy elements and we change the location of the helium phase transition to explore the sensitivity of the results to different model input parameters.

We run optimizations for the 3 different equations of state for hydrogen and helium explored in this work. It is important to note that we started each one of these runs with the same model, the same initial conditions and the same space of parameters to vary, but changing only the equation of state for hydrogen and helium. Figure 9 shows that Jupiter’s internal structure

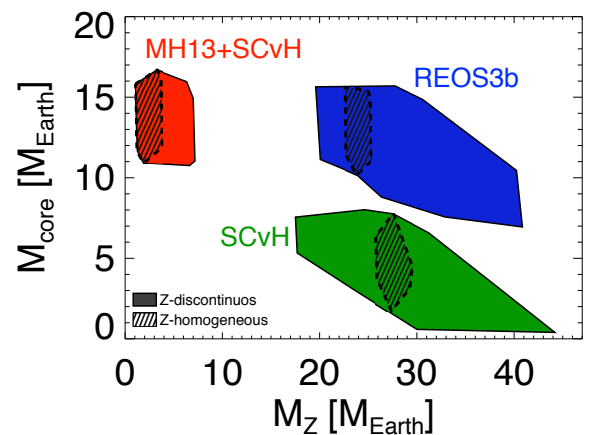


Fig. 9. The areas in the mass of the core and heavy elements space correspond to solutions found within 2σ and different equations of state for H and He: SCvH (green), MH13+SCvH (red) and REOS3b (blue area). Results found with Z-homogeneous are the areas within the dashed lines and correspond to a subgroup of the Z-discontinuous solutions (as will be in all the figures from now on).

is extremely sensitive to the equation of state adopted, as expected from the differences in thermal profiles shown in static models (section 4.1). The different equations of state lead to a completely different set of solutions that do not intersect with

each other. While SCvH leads to an interior of Jupiter with a small core and a large amount of heavy elements, results found with REOS3b indicate a much larger mass of heavy elements in general: a large core and a large abundance of heavy elements, and MH13+SCvH leads to a large core and a very small amount of heavy elements in Jupiter's interior.

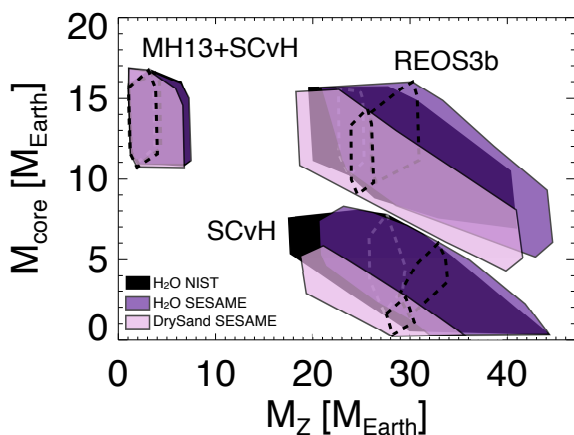


Fig. 10. Space of solutions obtained with different equations of state for H and He and for heavy elements. The equations of state for hydrogen and helium are indicated above the areas and the equations of state of heavy elements have different colors: H_2O NIST is black, Drysand SESAME is purple and H_2O NIST is pink.

Figure 10 shows that Jupiter's structure is also sensitive to the equation of state for heavy elements adopted in the model (section 3.3).

For REOS3b both M_{core} and M_Z get smaller when using dry sand SESAME, while the mass of heavy elements increase when using H_2O SESAME, when compared with results found with H_2O NIST EOS. For SCvH M_{core} is smaller for dry sand SESAME and M_Z is also smaller for the same core masses in comparison to results found with H_2O NIST EOS. MH13+SCvH is less sensitive to changes in the EOS for heavy elements.

We tested the sensitivity of the results to different P_{sep} . Figure 11 shows that when P_{sep} moves from larger (4Mbar) to lower pressures (0.8Mbar) more solids are found in the core.

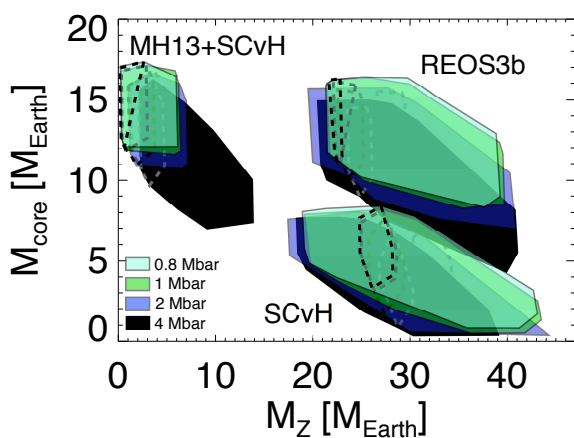


Fig. 11. Results of optimization models with different equations of state for H and He and changing the location of the P_{sep} : 4Mbar (black), 2 Mbar (blue), 1 Mbar (green) and 0.8 Mbar (light-blue).

4.3. Discussion: Sensitivity to internal energy calculations

REOS.3 tables were constructed with a different scheme than SCvH tables. Their internal energies are not the same, not even in the H_2 regime. We constructed REOS3b tables changing the zero point of the specific internal energy to coincide with SCvH values at $T=60$ K and $\rho = 10^{-3}$ g/cm³, but the difference between the tables differ when we move to different temperatures. Results by Militzer & Ceperley (2001); Militzer (2013); Militzer & Hubbard (2013) also show differences with SCvH internal energies. They found that SCvH model consider lower temperature intervals for the ionization of hydrogen atoms, which causes the discrepancy with their internal energies results.

To test the sensitivity of the internal structure calculations to differences in the internal energy derivation, we calculated a second equation of state based on REOS.3 results, in which we calculated the difference between the REOS.3 and SCvH and shifted the internal energies at all densities accordingly in order to make them coincide at $\rho = 10^{-3}$ g/cm³ for *all* temperatures. We then calculated the entropy for each point of the table and performed static and optimized calculations. We called these new tables REOS3sc (shown in appendix A). Figure 12 shows Jupiter's internal structure calculated with REOS3b and REOS3sc. The differences in internal energy lead to a difference in the entropies which affect the thermal profile.

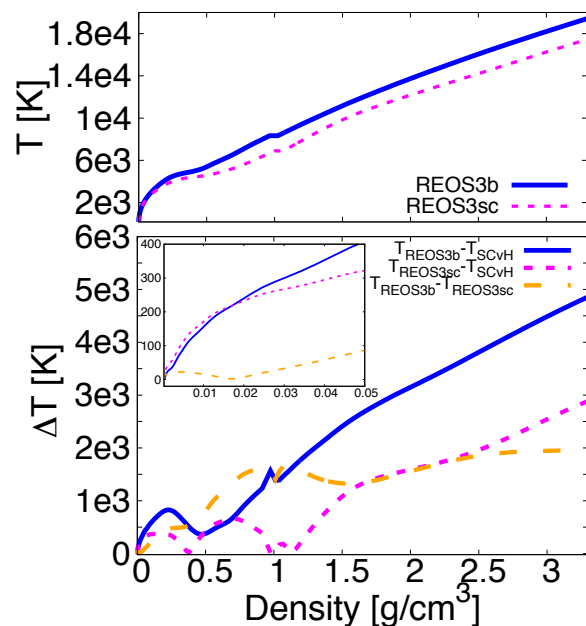


Fig. 12. Thermal profile calculated for Jupiter when using two equations of state derived using different internal energies. Top panel shows temperature vs. density, where blue is REOS3b and dashed magenta line was obtained with our test case the REOS3sc eos. Lower panel shows the differences in temperatures derived with the different equations of state: blue line is the difference between REOS3b and SCvH, dashed magenta line is the difference between REOS3sc and SCvH and orange line is the difference between REOS3b and REOS3sc.

The different temperatures in the interior of the planet lead to different core mass and mass of heavy elements derived in the optimized calculations. Figure 13 shows the solutions found with both equations of state, which shows that results are very sensitive to the internal energy and entropy calculations.

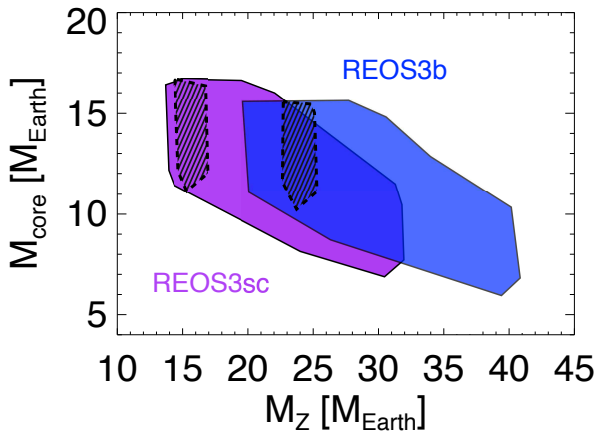


Fig. 13. Differences between the results obtained with REOS3b and REOS3sc equations of state.

5. Conclusions

Jupiter reservoir of heavy elements is key to understand the origin of our Solar system. Nevertheless, the distribution and amount of heavy elements in its interior is difficult to constrain and degeneracies arise depending on assumed observational constraints and model parameters in interior structure calculations. We present Jupiter optimized models, where the mass of the core and the mass of heavy elements are adjusted to reproduce Jupiter’s radius, J_2 and J_4 . We show how our solutions change drastically with the EOS for hydrogen and helium and also explore the sensitivity to heavy elements equations of state, separation between metallic and molecular envelope and distribution of heavy elements in Jupiter’s interior.

We adopt two different models for Jupiter, both scenarios consider helium phase separation and correspondingly different helium abundance in the outer and deeper layer. The difference is in the heavy elements distribution: one scenario has an homogeneous distribution of heavy elements and its mass mixing ratio is adjusted according to the observables. In the second scenario, Jupiter has different compositions of heavy elements in the two layers and the difference in the abundance in the outer and deeper envelope (ΔZ) is adjusted to find solutions that best reproduce Jupiter observational data. Allowing a change in heavy elements between the two layers adds a degree of freedom to the problem, which grants more solutions in the M_Z - M_{core} space. The pressure at which the separation between the two envelope layers occurs affects the solutions. This separation occurs between 0.8 and 4 Mbar, according to Morales et al. (2013) helium rain studies. We find that M_Z decreases and M_{core} increases when P_{sep} moves from high to low pressures.

Based on the works by Saumon et al. (1995); Militzer & Hubbard (2013); Becker et al. (2014), we explored hydrogen and helium equations of state and show that significant differences remain in these EOSs, although they match experimental data obtained by compression experiments along a Hugoniot. Some of the differences come from internal energy and entropy calculations. We show how small changes in the internal energy lead to differences in the entropy calculated which in turn affect the thermal profile and the estimation of the mass of the core and heavy elements. This explains differences seen in recently published interior models of the planet. Jupiter internal structure has a much large temperature when using REOS3b than with SCvH. For densities $\rho > 0.22246 \text{ g/cm}^3$, MH13+SCvH leads to

much lower temperatures than the other two EOS. This differences in the thermal structure lead to differences in the derived M_{core} and M_Z . MH13+SCvH allows larger M_{core} and smaller M_Z while REOS3b has larger M_{core} but similar M_Z than results find with SCvH.

In our baseline simulations, MH13+SCvH leads to M_{core} between 11 and 17 M_{Earth} , in agreement with results by Militzer & Hubbard (2013) and the preferred model of Hubbard & Militzer (2016). REOS3b leads to M_{core} between 7 and 16 M_{Earth} , larger than estimations by Nettelmann et al. (2012) and Becker et al. (2014). While their preferred model has $P_{sep} \geq 4$ Mbar, our models put the separation between Z_{atm} and Z_{deep} in the same place as the helium phase transition, between 0.8 and 4 Mbar (Morales et al. 2013) and the baseline simulations have $P_{sep}=2$ Mbar. When comparing the results at $P_{sep}=4$ Mbar we find a lower limit for the mass of the core of 4 M_{Earth} , consistent with the small core hypothesis showed by Nettelmann et al. (2012) and Becker et al. (2014) for the same case. Other small differences are due to different model parameters such us the temperature at the 1 bar limit, equation of state used for solids and differences in entropy calculation.

The equation of state for the heavy elements is also relevant. We study three different equations of state for rocks and water. Dry sand SESAME (Lyon & Johnson 1992) allows smaller M_{core} , while M_Z increase when using H_2O SESAME (Lyon & Johnson 1992) when compared with solutions obtained with hot water NIST EOS (Valencia et al. 2013).

Our results help in the interpretation of Jupiter observational data. Its gravitational moments changed from the first pre-Juno data (Campbell & Synnott 1985) to the constrains we have today (Jacobson, 2013). They also change according to the dynamics and rotation of Jupiter adopted in the model. Given the relatively large scatter in the gravitational moments of Jupiter inferred between 1985 and today, in our baseline simulations we chose to use conservative 2σ error bars based on the published value of Campbell & Synnott (1985) which encompass all of these values. We also show how different Js lead to different estimations of the core and heavy elements masses having a difference of up to $4M_{Earth}$ in M_{core} and $\sim 6M_{Earth}$ in M_Z for REOS3b and SCvH. Our preferred results have larger J_6 than the ones currently published. Juno mission will provide more accurate data, improving our knowledge of Jupiter internal structure.

Acknowledgements

We thank Bill Hubbard and Naor Movshovitz for valuable comments and for providing model comparisons to estimate the error in the Js calculation. We also thank Andreas Becker, Nadine Nettelmann and Burkhard Militzer for fruitful discussions regarding equations of state. Computations have been done on the ‘Mesocentre SIGAMM’ machine, hosted by Observatoire de la Cote d’Azur.

References

- Atkinson, D. H., Pollack, J. B., & Seiff, A. 1998, *J. Geophys. Res.*, 103, 22911
- Bahcall, J.N. & Pinsonneault, M.H. 1995, *Rev. Mod. Phys.* 67, 781–808.
- Baraffe, I., Chabrier, G., Fortney, J., & Sotin, C. 2014, *Protostars and Planets VI*, 763
- Becker, A., Winfried, L., Fortney, J., Nettelmann, N., Schottler, M. & Redmer, R. 2014, *ApJS*, 215, 21
- Belov, S. I., Boriskov, G. V., Bykov, A. I., et al. 2002, *Soviet Journal of Experimental and Theoretical Physics Letters*, 76, 433
- Brygoo, S., Millot, M., Loubeyre, P., et al. 2015, *Journal of Applied Physics*, 118, 195901

- Boriskov, G. V., Bykov, A. I., Il'KaeV, R. I., et al. 2003, *Physics - Doklady*, 48, 553
- Caillabet, L., Mazevet, S., & Loubeyre, P. 2011, *Phys. Rev. B*, 83, 094101
- Campbell, J.K., Synnott, S.P. 1985, *Astron. J.* 90, 364.
- Celliers, P. M., Loubeyre, P., Eggert, J. H., et al. 2010, *Physical Review Letters*, 104, 184503
- Collins, G. W., da Silva, L. B., Celliers, P., et al. 1998, *Science*, 281, 1178
- Eggert, J., Brygoo, S., Loubeyre, P., et al. 2008, *Physical Review Letters*, 100, 124503
- Fortney, J. J., & Nettelmann, N. 2010, *Space Sci. Rev.*, 152, 423
- French, M., Mattsson, T. R., Nettelmann, N., & Redmer, R. 2009, *PhRvB*, 79, 054107
- Galanti, E., & Kaspi, Y. 2016, *ApJ*, 820, 91
- Grishechkin, S. K., Gruzdev, S. K., Gryaznov, V. K., et al. 2004, *Soviet Journal of Experimental and Theoretical Physics Letters*, 80, 398
- Guillot, T., Chabrier, G., Morel P. & Gautier, D. 1994, *Icarus*, 112, 354–367.
- Guillot, T., & Morel, P. 1995, *A&AS*, 109, 109–123
- Guillot, T. 1999, *Planetary and Space Science*, 47, 1183
- Guillot, T., Stevenson, D. J., Hubbard, W. B., & Saumon, D. 2004, *Jupiter. The Planet, Satellites and Magnetosphere*, 1, 35
- Guillot T., and Gautier D *Giant Planets*. In: Gerald Schubert (editor-in-chief) *Treatise on Geophysics*, 2nd edition, Vol 10. Oxford: Elsevier; 2015. p. 529-557
- Helled, R., Bodenheimer, P., Podolak, M., et al. 2014, *Protostars and Planets VI*, 643
- Hicks, D. G., Boehly, T. R., Celliers, P. M., et al. 2009, *Phys. Rev. B*, 79, 014112
- Holmes, N. C., Ross, M., & Nellis, W. J. 1995, *Phys. Rev. B*, 52, 15835
- Hubbard, W.B. 1982, *Icarus* 52, 509.
- Hubbard, W. B. 2012, *ApJ*, 756, L15
- Hubbard, W. B. 2013, *ApJ*, 768, 43
- Hubbard, W. B., & Militzer, B. 2016, *ApJ*, 820, 80
- Kaspi, Y., Hubbard, W. B., Showman, A. P., & Flierl, G. R. 2010, *Geophys. Res. Lett.*, 37, L01204
- Knudson, M. D., Hanson, D. L., Bailey, J. E., et al. 2004, *Phys. Rev. B*, 69, 144209
- Knudson, M. D., & Desjarlais, M. P. 2009, *Physical Review Letters*, 103, 225501
- Leconte, J., & Chabrier, G. 2012, *A&A*, 540, A20
- Lindal, G. F. Mar. 1992, *AJ*103, 967-982.
- Loubeyre, P., Brygoo, S., Eggert, J., et al. 2012, *Phys. Rev. B*, 86, 144115
- Lyon S. & Johnson J. , 1992, LANL Report LA-UR-92-3407, Los Alamos.
- Mankovich, C., Fortney, J. J., & Moore, K. L. 2016, arXiv:1609.09070
- Militzer, B., & Ceperley, D. M. 2001, *Phys. Rev. E*, 63, 066404
- Militzer, B., Hubbard, W. B., Vorberger, J., Tamblyn, I., & Bonev, S. A. 2008, *ApJ*, 688, L45
- Militzer, B. 2006, *Physical Review Letters*, 97, 175501
- Militzer, B. 2009, *Phys. Rev. B*, 79, 155105
- Militzer, B. 2013, *Phys. Rev. B*, 87, 014202
- Militzer, B., & Hubbard, W. B. 2009, *Ap&SS*, 322, 129
- Militzer B. & Hubbard W. B. 2013, *ApJ*, 774, 148.
- Morales, M. A., Hamel, S., Caspersen, K., & Schwegler, E. 2013, *Physical Review B*, 87, 174105
- Nellis, W. J., Mitchell, A. C., van Thiel, M., et al. 1983, *Journal of Chemical Physics*, 79, 1480
- Nellis, W. J., Holmes, N. C., Mitchell, A. C., et al. 1984, *Physical Review Letters*, 53, 1248
- Nettelmann, N., Holst, B., Kietzmann, A., et al. 2008, *ApJ*, 683, 1217-1228
- Nettelmann, N., Becker, A., Holst, B., & Redmer, R. 2012, *ApJ*, 750, 52
- Nettelmann, N., Fortney, J. J., Moore, K., & Mankovich, C. 2015, *MNRAS*, 447, 3422
- Pollack, J. B., Hubickyj, O., Bodenheimer, P., et al. 1996, *Icarus*, 124, 62
- Saul, A., & Wagner, W. 1989, *JPCRD*, 18, 1537
- Saumon, D., Chabrier, G. & van Horn, H. M. 1995 *ApJS*, 99, 713.
- Saumon, D., & Guillot, T. 2004, *ApJ*, 609, 1170
- Valencia, D., Guillot, T., Parmentier, V., & Freedman, R. S. 2013, *ApJ*, 775, 10
- Vazan, A., Helled, R., Podolak, M., & Kovetz, A. 2016, *ApJ*, 829, 118
- von Zahn, U., Hunten, D.M., Lehman, G. 1998. *J. Geophys. Res.* 103, 22815–22830.

Appendix A: Equations of state

We present the equations of state derived in this paper. We note that the equations of state were tested and used only in a restricted range of pressures (10^6 to 10^{14} dyn/cm²) and temperatures (100 to 10^5 K) relevant for modeling Jupiter's internal structure. There are some deviations between the entropies calculated and those in SCvH table for $\log(s) < 8.6$ in the hydrogen tables and for $\log(s) < 8.2$ and densities $\log(\rho) < -5$ in the helium tables.

All the tables in this appendix are available in their entirety in the online journal. A portion is shown here for guidance regarding their form and content.

Table A.1. MH13+SCvH table for hydrogen.

$\log(P)$ [dyn/cm ²]	$\log(T)$ [K]	$\log(\rho)$ [g/cm ³]	$\log(s)$ [erg/gK]
4.0000000000000000	2.2500	-5.8654028904134083	8.9259253894161983
4.1500000000000004	2.2500	-5.7154039997492951	8.9185239042839068
4.3000000000000007	2.2500	-5.5654055482155513	8.9109945018226053
4.4500000000000011	2.2500	-5.4154076999882692	8.9033332403514844
4.6000000000000014	2.2500	-5.2654107675309119	8.8955336686414146
4.7500000000000018	2.2500	-5.1154150888124521	8.8875914762240953
4.9000000000000021	2.2500	-4.9654211956861642	8.8795012650122480
5.0500000000000025	2.2500	-4.8154298213730833	8.8712572711005073

Table A.2. REOS3b table for hydrogen.

$\log(P)$ [dyn/cm ²]	$\log(T)$ [K]	$\log(\rho)$ [g/cm ³]	$\log(s)$ [erg/gK]
7.50000000	1.77815127	-1.74398792	8.51118183
7.57499981	1.77815127	-1.60381353	8.48558712
7.64999962	1.77815127	-1.40540540	8.43856716
7.72499943	1.77815127	-1.30222011	8.40594292
7.79999924	1.77815127	-1.25477469	8.38819885
7.87499905	1.77815127	-1.22213173	8.37435246
7.94999886	1.77815127	-1.19594634	8.36197186
8.02499866	1.77815127	-1.17360163	8.35033607

Table A.3. REOS3b table for helium.

$\log(P)$ [dyn/cm ²]	$\log(T)$ [K]	$\log(\rho)$ [g/cm ³]	$\log(s)$ [erg/gK]
4.50000000	1.77815127	-4.59566355	8.48160362
4.57499981	1.77815127	-4.52066803	8.47642231
4.64999962	1.77815127	-4.44567299	8.47117710
4.72499943	1.77815127	-4.37067795	8.46586895
4.79999924	1.77815127	-4.29568529	8.46049404
4.87499905	1.77815127	-4.22069359	8.45505142
4.94999886	1.77815127	-4.14570236	8.44953823
5.02499866	1.77815127	-4.07071352	8.44405270

Table A.4. REOS3sc table for hydrogen.

$\log(P)$ [dyn/cm ²]	$\log(T)$ [K]	$\log(\rho)$ [g/cm ³]	$\log(s)$ [erg/gK]
7.50000000	1.77815127	-1.74398792	8.49107647
7.57499981	1.77815127	-1.60381353	8.46421719
7.64999962	1.77815127	-1.40540540	8.41470623
7.72499943	1.77815127	-1.30222011	8.38014793
7.79999924	1.77815127	-1.25477469	8.36175156
7.87499905	1.77815127	-1.22213173	8.34656525
7.94999886	1.77815127	-1.19594634	8.33196449
8.02499866	1.77815127	-1.17360163	8.31901360

Table A.5. REOS3sc table for helium.

$\log(P)$ [dyn/cm ²]	$\log(T)$ [K]	$\log(\rho)$ [g/cm ³]	$\log(s)$ [erg/gK]
4.50000000	1.77815127	-4.59566355	8.49313259
4.57499981	1.77815127	-4.52066803	8.48808765
4.64999962	1.77815127	-4.44567299	8.48298264
4.72499943	1.77815127	-4.37067795	8.47781658
4.79999924	1.77815127	-4.29568529	8.47258949
4.87499905	1.77815127	-4.22069359	8.46729851
4.94999886	1.77815127	-4.14570236	8.46194172
5.02499866	1.77815127	-4.07071352	8.45651817